'95.10.-3 (filed)

Nuclear Physics A462 (1987) 491-526
North-Holland, Amsterdam

p - p

INFINITE ORDER SUMMATION OF PARTICLE-PARTICLE RING DIAGRAMS IN A MODEL-SPACE APPROACH FOR NUCLEAR MATTER*

H.Q. SONG[1], S.D.YANG[2] and T.T.S. KUO

Department of Physics, The State University of New York at Stony Brook, Stony Brook, NY 11794, USA

Received 28 February 1986
(Revised 25 July 1986)

Abstract: A ring diagram model-space nuclear matter theory is formulated and applied to the calculation of the binding energy per nucleon (BE/A), saturation Fermi momentum (k_F) and incompressibility coefficient (K) of symmetric nuclear matter, using the Paris and Reid nucleon-nucleon potentials. A model space is introduced where all nucleons are restricted to have momentum $k \leq k_M$, typical values of k_M being $\sim 3.2\ \text{fm}^{-1}$. Using a model-space Hartree-Fock approach, self-consistent single particle spectra are derived for holes ($k \leq k_F$) and particles with momentum $k_F < k \leq k_M$. For particles with $k > k_M$, we use a free particle spectrum. Within the model space we sum up the particle-particle ring diagrams (both forward- and backward-going) to all orders. A rather simple expression for the energy shift ΔE_0^{pp} is obtained, namely ΔE_0^{pp} is expressed as integrals involving the trace of $Y(\lambda)Y^{+}(\lambda)G^{M}$ where G^M is the model-space reaction matrix, the Y's are transition amplitudes obtained from solving RPA-type secular equations and λ is a strength parameter to be integrated from 0 to 1. We have used angle-average approximations in our calculations, and in this way different partial wave channels are decoupled. For the $^3S_1$-$^3D_1$ channel, the effect of the ring diagrams is found to be particularly important. The inclusion of the ring diagrams has largely increased the role of the tensor force in determining the nuclear matter saturation properties, and consequently we obtain saturation densities which are significantly lower than those given by most other calculations. For the Paris potential, our results for BE/A, k_F and K are respectively 17.38 MeV, 1.42 fm^{-1} and 96.3 MeV. For the Reid potential, the corresponding results are 15.15 MeV, 1.30 fm^{-1} and 110.7 MeV. Our calculated values for the binding energy per nucleon and saturation density are *both* in rather satisfactory agreement with the corresponding empirical values.

1. Introduction

A primary aim of nuclear matter theory is to provide a microscopic derivation of the empirical nuclear matter properties such as the binding energy per nucleon BE/A, saturation density ρ_0 (or saturation Fermi momentum k_F) and the incompressibility coefficient K. In fact there have been a very large amount of works [1-6]) in

---

* Supported in part by the United States Department of Energy under contract number DE-AC02-76ER13001.

[1] Permanent address: Institute of Nuclear Research, Academia Sinica, P.O. Box 8204, Shanghai, the People's Republic of China.

[2] Permanent address: Dept. of Physics, Jilin University, Changchun, the People's Republic of China.

375-9474/87/$03.50

this area, and certainly nuclear matter theory has played a very important role in nuclear physics. A long standing difficulty in nuclear matter theory has been the inability of almost all theoretical calculations in obtaining BE/A and ρ_0 which are in simultaneous agreement with the corresponding empirical values. ^{7}) (The accepted empirical values for BE/A, ρ_0 and K are respectively ~16 MeV, ~0.17 fm^{-1} and ~200 MeV. Recently Brown and Osnes ^{8}) have suggested that K should be considerably smaller, being ~110 MeV.) Frequently, if the calculated BE/A is satisfactory, then the calculated ρ_0 is too high. And if the calculated ρ_0 is more or less correct, then the calculated BE/A is usually far from being adequate.

There have been a number of developments aimed at resolving the above discrepancy. Many believe that a major rethinking of the two-body nucleon-nucleon(NN) potential is in order ^{9}). The concern here is primarily that the usual practice of employing only a two-body NN potential which fits the NN scattering data in nuclear matter calculations is indequate in reproducing the empirical properties of nuclear matter. In fact, a recent nuclear matter calculation by Kuo, Ma and Vinh Mau ^{10}) indicated that a small three-body interaction, cast in the form of a density dependent two-body interaction, was quite helpful in bringing the calculated values of both the BE/A and ρ_0 to reasonable agreement with the empirical results. Another line of developments is in the direction of refining the many-body methods used in nuclear matter calculations. Many elaboorate many-body methods have been advocated, such as the exp S approach ^{11}), the Green function approach ^{3}), the hyper-netted chain approach ^{12}), and the model-space approach ^{13}). All these approaches are formulated to give a more accurate nuclear matter theory than the prototypical lowest-order BHF theory with a discontinuous single-particle spectrum. The above theories are all non-relativistic. It should be noted that Shakin and his collaborators ^{14}) have recently proposed a highly promising relativistic nuclear matter theory, suggesting that relativistic effects may be very important in reproducing the correct nuclear matter saturation density.

The main purpose of the present study is a rather confined one. Recently, Yang, Heyer and Kuo [YHK] ^{15}) have proposed a convenient and rigorous method for summing up certain classes of ring diagrams to all orders for the calculation of ground state energies of general many-body systems. It seems to be of much interest to investigate the application of this method to nuclear matter calculations. In particular, the long range correlations arising from ring diagrams correlations in nuclear matter seem not to have been studied in a general way in existing nuclear matter calculations, and we feel that they may play an important role in determining the nuclear matter bulk properties BE/A, ρ_0 and K and the inter-relation among them. The combination of the YHK ring diagram method and the model-space nuclear matter approach ^{13}) may provide a new and suitable formulation for studying such long range correlations in nuclear matter. In this paper, we formulate and carry out model-space nuclear matter calculations where within a chosen model space the particle-particle ring diagrams of nuclear matter are summed to all orders. The effect of these ring diagrams on BE/A, ρ_0 and K are, in particular, examined.

Our calculation is also motivated by the following physical intuition. In treating many-body problems, it is definitely of great importance to choose a "good" single particle (s.p.) potential, in the sense that this potential should be a good representation of the actual average nuclear field felt by a nucleon in the nuclear medium under consideration. From this view point, the conventional BHF s.p. spectrum is certainly unsatisfactory because it has a large artificial discontinuity at the Fermi surface k_F [3]. We will adopt the model-space approach of Ma and Kuo [13] for determining the s.p. potential. This approach advocates the following partition concept. A model space P is defined as a configuration space where all nucleons are restricted to have momentum $k \leq k_M$, k_M being the momentum space boundary of P. As is discussed later, a typical value for k_M is $\sim 3\ \text{fm}^{-1}$. It is then conjectured that nuclear correlations with their intermediate states outside P can be adequately treated with the usual G-matrix approach. In fact, these correlations are primarily due to the short-range repulsion of the NN potential. Nuclear correlations whose intermediate states are inside P should be treated more thoroughly, such as including the ring diagrams to all orders. Based on the above concept our nuclear matter calculations are carried out in the following two-step approach. First, we choose a model space P and calculate self-consistently the model-space reaction matrix and s.p. spectrum. Then, within P, we sum up the particle-particle ring diagrams to all orders using the YHK method. Calculations are carried out using both the Paris [16] and the Reid [17] NN potentials.

The present work is a continuation of the model-space BHF (MBHF) nuclear matter calculations of Ma and Kuo [13], and Kuo, Ma and Vinh Mau [10]*. In their calculations, a space P was first chosen and within P a continuous s.p. spectrum was determined self-consistently. Then the MBHF calculations were carried out by summing up only the upward-going G-matrix ladder diagrams within P to all orders. The binding energies given by these MBHF calculations are already fairly satisfactory. Hence there is the concern that nuclear matter may become overly bound when we include ring diagrams to all orders in our calculations. This concern in fact appears to be a very cogent one because in our model space approach the s.p. spectrum is continuous. Thus there is either no gap between particle and hole states, or a relatively small gap at k_F if one chooses to treat the hole s.p. spectrum slightly differently from the particle one [13]. Consequently it is relatively easy to have particle–hole excitations, and the effect of the ring diagrams for such model-space calculations may be particularly large or even overly so. Needless to say, it is this concern which has provided us with additional motivation for carrying out the present nuclear matter calculations.

p-h ?

---

* Several calculational details of the MBHF method for nuclear matter calculations were not given in refs. [10,13]. We will describe them in this paper.

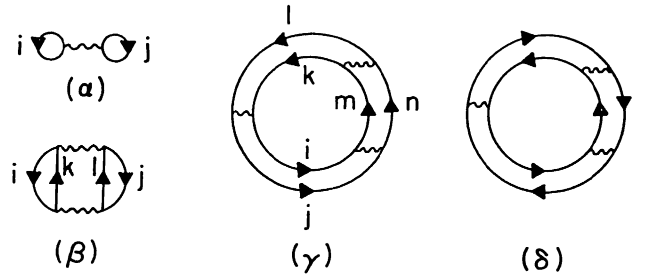

Fig. 1. Low-order linked diagrams of the energy shift $\Delta E_0 = E_0 - W_0$. Each wave line vertex denotes an anti-symmetrized vertex of V.

The contributions to ΔE_0 from diagrams (α), (β) and (γ) of fig. 1 are[15] respectively

$$\Delta E_0^{\mathrm{pp}}(1) = \frac{-1}{2\pi i}\int_{-\infty}^{\infty} \mathrm{d}\omega\, \mathrm{e}^{i\omega 0^+} F_{ij}(\omega)\, \bar{V}_{ijij}\,, \tag{2.1}$$

$$\Delta E_0^{\mathrm{pp}}(2) = \frac{-1}{2\pi i}\int_{-\infty}^{\infty} \mathrm{d}\omega\, \mathrm{e}^{i\omega 0^+} \tfrac{1}{2} F_{ij}(\omega)\, \bar{V}_{ijkl} F_{kl}(\omega)\, \bar{V}_{klij}\,, \tag{2.2}$$

$$\Delta E_0^{\mathrm{pp}}(3) = \frac{-1}{2\pi i}\int_{-\infty}^{\infty} \mathrm{d}\omega\, \mathrm{e}^{i\omega 0^+} \tfrac{1}{3} F_{ij}(\omega)\, \bar{V}_{ijkl} F_{kl}(\omega)\, \bar{V}_{klmn} F_{mn}(\omega)\, \bar{V}_{mnij}\,, \tag{2.3}$$

where repeated indices are summed over all the s.p. states without restriction (e.g., we sum over both $i > j$ and $i < j$), and F_{ij} is the unperturbed pair propagator given by

$$\boxed{F_{ij}(\omega) = \frac{\bar{n}_i \bar{n}_j}{\omega - (\varepsilon_i + \varepsilon_j) + i0} - \frac{n_i n_j}{\omega - (\varepsilon_i + \varepsilon_j) - i0}\,.} \tag{2.4}$$

The matrix elements of $\bar{V}$ are defined as

$$\bar{V}_{ijkl} = \tfrac{1}{2}(V_{ijkl} - V_{ijlk})\,. \tag{2.5}$$

Note that V_{ijkl} is the simple product matrix element $\int \mathrm{d}^3 r_1\, \mathrm{d}^3 r_2\, \phi_i^*(\boldsymbol{r}_1)\phi_j^*(\boldsymbol{r}_2) \cdot V(r_{12})\phi_k(\boldsymbol{r}_1)\phi_l(\boldsymbol{r}_2)$. In eq. (2.4), $n_i = 1$ if $k_i < k_F$ and $= 0$ if $k_i > k_F$, and $\bar{n}_i \equiv 1 - n_i$. In addition, the factors $\pm i0$ in the denominators are abbreviations for $\pm i\eta$ in the limit of $\eta \to 0^+$. (0^+ here and in eqs. (2.1) to (2.3) denotes an infinitesimally small positive quantity.) This notation will be used from now on.

In this way, the particle-particle (pp) ring diagrams such as those shown by diagrams (α), (β) and (γ) of fig. 1 can be summed up to all orders, leading to

$$\Delta E_0^{\mathrm{pp}} = \frac{-1}{2\pi i}\int_{-\infty}^{\infty} \mathrm{d}\omega\, \mathrm{e}^{i\omega 0^+} \operatorname{tr}\left(F\bar{V} + \tfrac{1}{2}(F\bar{V})^2 + \tfrac{1}{3}(F\bar{V})^3 + \cdots\right\}, \tag{2.6}$$

where the series inside the curly brackets form a logarithmic function. However, this is not so convenient for calculation. Let us introduce a strength parameter λ, and convert eq. (2.6) into

$$\Delta E_0^{\mathrm{pp}} = \frac{-1}{2\pi i}\int_0^1 \frac{\mathrm{d}\lambda}{\lambda}\int_{-\infty}^{\infty} \mathrm{d}\omega\, \mathrm{e}^{i\omega 0^+}\, \mathrm{tr}\,\{\lambda F\bar{V} + (\lambda F\bar{V})^2 + (\lambda F\bar{V})^3 + \cdots\}\,. \tag{2.7}$$

It is of interest to note that the introduction of the strength parameter λ makes the quantity inside the curly brackets a simple geometric series. This is not only computationally convenient but also physically desirable - it tells us that the ground state energy shift ΔE_0^{pp} is dependent on how the many-body system evolves from a non-interacting system ($\lambda = 0$) to a fully intereacting system ($\lambda = 1$).

We now introduce a λ-dependent particle-particle Green function $G^{\mathrm{pp}}(\omega, \lambda)$ defined by

$$G^{\mathrm{pp}}_{ijkl}(\omega, \lambda) = F_{ij}(\omega)\delta_{ij,kl} + F_{ij}(\omega)\lambda \bar{V}_{ijmn}(G^{\mathrm{pp}}_{mnkl}(\omega, \lambda)\,. \tag{2.8}$$

Then ΔE_0^{pp} of eq. (2.7) can be cast into the compact form

$$\Delta E_0^{\mathrm{pp}} = \frac{-1}{2\pi i}\int_0^1 \frac{\mathrm{d}\lambda}{2\pi i}\int_{-\infty}^{\infty} \mathrm{d}\omega\, \mathrm{e}^{i\omega 0^+}\, \mathrm{tr}\,\{G^{\mathrm{pp}}(\omega, \lambda)\bar{V}\lambda\}\,. \tag{2.9}$$

An alternative approach is via the λ-dependent generalized reaction matrix $K^{\mathrm{pp}}(\omega, \lambda)$ defined by

$$K^{\mathrm{pp}}_{ijkl}(\omega, \lambda) \equiv \lambda \bar{V}_{ijkl} + \lambda \bar{V}_{ijmn} F_{mn}(\omega) K^{\mathrm{pp}}_{mnkl}(\omega, \lambda)\,. \tag{2.10}$$

Then ΔE_0^{pp} is given by

$$\Delta E_0^{\mathrm{pp}} = \frac{-1}{2\pi i}\int_0^1 \frac{\mathrm{d}\lambda}{\lambda}\int_{-\infty}^{\infty} \mathrm{d}\omega\, \mathrm{e}^{i\omega 0^+}\, \mathrm{tr}\,\{F(\omega)K^{\mathrm{pp}}(\omega, \lambda)\}\,. \tag{2.11}$$

The task now confronting us is how to actually calculate ΔE_0^{pp} for nuclear matter. The expressions (2.9) and (2.11) are both compact and appealing but it is more important to investigate whether they provide a convenient and practical scheme for actual calculations. Before investigating this question for nuclear matter, let us first point out that our ΔE_0^{pp} sums up the particle-particle ring diagrams to all orders, including diagrams (α), (β) and (γ) of fig. 1, and the general particle-particle ring diagram (i) of fig. 2. Thus we draw the general ring diagram in the circular form shown in fig. 2 to emphasize the fact that the two lines in each pair propagator can be either both particles ($>k_{\mathrm{F}}$) or both holes ($<k_{\mathrm{F}}$). Hence our present formulation includes contributions to ΔE_0 from repeated interactions between two hole lines (i.e. hole-hole correlations) to all orders and also ground-state correlation interactions connecting two particle to two hole lines to all orders. In contrast, only the repeated interactions between a pair of particle lines are included in the usual BHF type nuclear matter calculations, as illustrated by diagram (ii) of fig. 2.

We have found that it is more convenient in several aspects to use eq. (2.9) than eq. (2.11) for calculating ΔE_0^{pp}. This is because the frequency integration (i.e. $\int \mathrm{d}\omega$)

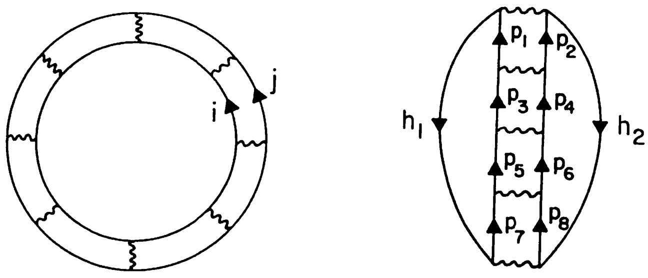

(i) (ii)

Fig. 2. (i) A general ring diagram included in the present work. Note that i and j can be either both particles ($>k_F$) or both holes ($<k_F$). (ii) A general diagram included in the usual BHF type nuclear matter calculations. Note that all p's are restricted to be $>k_F$, and h's $<k_F$.

in the former is considerably easier to carry out than in the latter. [15]) Hence, in the present work, we use the former scheme. To carry on the calculation, we first need to calculate the Green function G^{pp} and also find a way to perform the ω integration. A convenient way to proceed is to write G^{pp} in its Lehmann's representation, namely

$$G^{\mathrm{pp}}_{ijkl}(\omega,\lambda)=\sum_n \frac{X_n(ij,\lambda)X_n^*(kl,\lambda)}{\omega-\omega_n^+(\lambda)+i0}-\sum_m \frac{Y_m(ij,\lambda)Y_m^*(kl,\lambda)}{\omega-\omega_m^-(\lambda)-i0}, \qquad (2.12)$$

where

$$\omega_n^+(\lambda)=E_n^{A+2}(\lambda)-E_0^A(\lambda), \qquad (2.12a)$$

$$\omega_m^-(\lambda)=E_0^A-E_m^{A-2}(\lambda), \qquad (2.12b)$$

$$X_n(ij,\lambda)=\langle\Psi_0^A(\lambda)|a_ja_i|\Psi_n^{A+2}(\lambda)\rangle, \qquad (2.12c)$$

$$Y_m(ij,\lambda)=\langle\Psi_m^{A-2}(\lambda)|a_ja_i|\Psi_0^A(\lambda)\rangle. \qquad (2.12d)$$

Here the eigenfunctions and eigenvalues are defined by $(H_0+\lambda H_1)\Psi_0^A(\lambda)=E_0^A(\lambda)\Psi_0^A(\lambda)$, $(H_0+\lambda H_1)\Psi_n^{A+2}(\lambda)=E_n^{A+2}(\lambda)\Psi_n^{A+2}(\lambda)$, and similarly for $\Psi_m^{A-2}(\lambda)$ and $E_m^{A-2}(\lambda)$. Substituting the above into eq. (2.9) leads to the result [15])

$$\Delta E_0^{\mathrm{pp}}=\int_0^1\frac{\mathrm{d}\lambda}{\lambda}\sum_{\substack{m\\(A-2)}}\sum_{ijkl}Y_m(ij,\lambda)Y_m^*(kl,\lambda)\bar{V}_{klij}\lambda, \qquad (2.13)$$

where the amplitudes Y_m are calculated from the RPA-type equation

$$\sum_{ef}\{(\varepsilon_i+\varepsilon_j)\delta_{ij,ef}+(\bar{n}_i\bar{n}_j-n_in_j)\lambda\bar{V}_{ijef}\}Y_m(ef,\lambda)=\omega_m^-(\lambda)Y_m(ij,\lambda). \qquad (2.14)$$

Note that the factor $(\bar{n}_i\bar{n}_j-n_in_j)$ can also be written as $(1-n_i-n_j)$. It should be emphasized that in eqs. (2.13) and (2.14) the summations are unrestricted, namely the indices for the summations are in fact $i>j$ and $i<j$, and similarly for k, l, e and f. Some simplification may be effected by making use of the symmetry properties of $\bar{V}$ and Y_m as depicted by eqs. (2.5) and (2.12d). The convergence factor $\mathrm{e}^{i\omega 0^+}$ in

eq. (2.9) has played an important role in obtaining eq. (2.13) from eqs. (2.9) and (2.12). This factor enables us to convert the ω integral in eq. (2.9) into a contour integral closed in the upper ω plane. This point will be discussed in more detail when we introduce the model-space G-matrix. The normalization of the Y_m vectors of eqs. (2.12d) and (2.14) will play an important role in our calculation and we will discuss this matter in sects. 3 and 4.

For nuclear matter calculations, $\bar{V}$ in eqs. (2.13) and (2.14) represents the matrix elements of a NN potential such as the Paris or Reid potential. Both have very strong short range repulsions and hence their $\bar{V}$ matrix elements are generally positive and very large. ($\bar{V}$ becomes infinite, if the NN potential employed has a hard-core short range repulsion.) Thus eqs. (2.13) and (2.14) are clearly not suitable for applying to many-body problems with interactions having strong short range repulsions. (In fact these equations are undefined in the case of hard-core NN potentials.) Some type of G-matrix partial summations are needed to take care of the strong short-range NN correlations. There is another difficulty. As it stands, eq. (2.14) is a matrix equation of infinite dimension. This is because its indices i, j, e and f run over all the s.p. states, of which there are infinitely many. (For nuclear matter, its s.p. states are continuum plane-wave states with momentum from 0 to ∞.) Thus eq. (2.14), as it stands, is not convenient for actual calculations. It would be very helpful if some form of truncation of it can be effected. Hence to carry out nuclear matter calculations based on the formulation outlined by eqs. (2.13) and (2.14), the two above mentioned difficulties must first be overcome.

3. Model space approach

We introduce here a model-space approach in order to reformulate the ring diagram method described in sect. 2 so that it can be expressed in terms of the model-space reaction matrix G^{M}. In this way, as will be seen shortly, we can overcome the two difficulties just mentioned. Let us divide the s.p. states into two groups: those with momentum $k > k_{\mathrm{M}}$ and those with $k \leq k_{\mathrm{M}}$. In drawing diagrams, the propagator corresponding to the former will be denoted by upward-going railed lines (see fig. 3). Our model space P is defined as a configuration space where all nucleons are restricted to have momentum $k \leq k_{\mathrm{M}}$, k_{M} being the momentum space

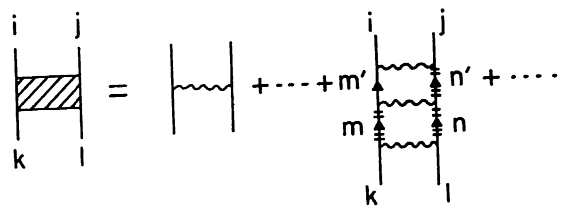

Fig. 3. Structure of the model space G^{M} matrix. Here the railed lines m, n and n' denote s.p. states with momentum $> k_{\mathrm{M}}$. m' denotes a s.p. state with momentum between k_{F} and k_{M}.

Furthermore, at least one line of each of the (u, v), (p, q) and (r, s) propagators must be outside the P space. In this way, we assure that there will be no double counting in combining particle–particle ring diagrams with $\bar{V}$ vertices into those with $\bar{G}^{\mathrm{M}}$ vertices. For example, any particle–particle ring diagram with three P-space propagators is included in the series shown in fig. 4. The sum of this entire series is a particle–particle ring diagram which is third order in $\bar{G}^{\mathrm{M}}$. Similarly all of the ring diagrams with four segments of P-space propagators are grouped together to form a corresponding ring diagram which is fourth order in $\bar{G}^{\mathrm{M}}$ vertex.

Thus we can now write ΔE_0^{pp} in two equivalent ways, either

$$\Delta E_0^{\mathrm{pp}} = \Delta E_0^{\mathrm{pp}}(1) + \Delta E_0^{\mathrm{pp}}(2) + \Delta E_0^{\mathrm{pp}}(3) + \cdots \tag{3.4}$$

or

$$\Delta E_0^{\mathrm{pp}} = \Delta E_0^{\mathrm{pp}}(1') + \Delta E_0^{\mathrm{pp}}(2') + \Delta E_0^{\mathrm{pp}}(3') + \cdots . \tag{3.5}$$

The various terms in eq. (3.4) have been given by eqs. (2.1) to (2.3). For example, $\Delta E_0^{\mathrm{pp}}(3)$ is third order in $\bar{V}$. In contrast, the various terms in eq. (3.5) are now expressed in terms of the $\bar{G}^{\mathrm{M}}$ interactions. For example, $\Delta E_0^{\mathrm{pp}}(3')$ is third order in $\bar{G}^{\mathrm{M}}$. $\Delta E_0^{\mathrm{pp}}(n')$ differs from $\Delta E_0^{\mathrm{pp}}(n)$ only in the replacement of the $\bar{V}$'s of the latter by the corresponding $\bar{G}^{\mathrm{M}}$'s and in the restriction on the summation of the indices. For example, $\Delta E_0^{\mathrm{pp}}(3')$ is given by

$$\Delta E_0^{\mathrm{pp}}(3') = \frac{-1}{2\pi i} \int_{-\infty}^{\infty} \mathrm{d}\omega \, \mathrm{e}^{i\omega 0^+} \frac{1}{3} \sum_{\substack{ijklmn \\ \varepsilon P}} F_{ij}(\omega) \bar{G}^{\mathrm{M}}_{ijkl}(\omega)$$
$$\times F_{kl}(\omega) \bar{G}^{\mathrm{M}}_{klmn}(\omega) F_{mn}(\omega) \bar{G}^{\mathrm{M}}_{mnij}(\omega) , \tag{3.6}$$

where we note that the indices $(i, j, \ldots n)$ are summed within the model space only.

Based on the above results, the steps leading to the eqs. (2.8) and (2.9) can be easily repeated using the $\bar{G}^{\mathrm{M}}$ vertices. Thus corresponding to eq. (2.9) we now have

$$\Delta E_0^{\mathrm{pp}} = \frac{-1}{2\pi i} \int_0^1 \frac{\mathrm{d}\lambda}{\lambda} \int_{-\infty}^{\infty} \mathrm{d}\omega \, \mathrm{e}^{i\omega 0^+} \operatorname{tr}_{\mathrm{P}} \{ G^{\mathrm{pp}}(\omega, \lambda) \bar{G}^{\mathrm{M}}(\omega) \lambda \} , \tag{3.7}$$

where the subscript P denotes that the trace is to be taken only within the model space P, and the model space reaction matrix $\bar{G}^{\mathrm{M}}$ has been given by eqs. (3.3) and (3.1). The Green function G^{pp} is now given in terms of $\bar{G}^{\mathrm{M}}$, namely

$$G^{\mathrm{pp}}_{ijkl}(\omega, \lambda) = F_{ij}(\omega) \delta_{ij,kl} + F_{ij}(\omega) \lambda \bar{G}^{\mathrm{M}}_{ijmn}(\omega) G^{\mathrm{pp}}_{mnkl}(\omega, \lambda) , \tag{3.8}$$

where note that the indices $i, j, \ldots$ and n are all within the model space P, and repeated indices are summed over freely (i.e. we sum over $m \gtrless n$). Thus eq. (3.8) is a model-space effective Dyson's equation. General properties of this type of the model-space effective Dyson's equations for the Green functions have been studied by Wu and Kuo. [19]

they are now calculated from a model space self-consistent equation of the RPA type namely

$$\sum_{ef}\{(\varepsilon_i+\varepsilon_j)\delta_{ij,ef}+(\bar{n}_i\bar{n}_j-n_in_j)\lambda L_{ijef}(\omega)\}\,Y_m(ef,\lambda)=\mu_m(\omega,\lambda)\,Y_m(ij,\lambda) \tag{3.14}$$

with the self-consistent condition for ω

$$\mu_m(\omega,\lambda)=\omega\equiv\omega_m^-(\lambda)\,, \tag{3.14a}$$

$$L_{ijef}(\omega)\equiv\bar{G}^{\mathrm{M}}_{ijef}(\omega)\,. \tag{3.14b}$$

Since the derivation and general properties of the above type of self-consistent equations have been given in detail elsewhere [19,20]), we will not give the details of the derivation of the above equations except to mention that they are obtained from eqs. (3.8), (2.12) and (2.4). In eq. (3.14), L is in general an irreducible vertex function containing both two-body and one-body terms (self-energy insertions). Here, as indicated by eq. (3.14b), we include in L only the two-body reaction matrix $\bar{G}^{\mathrm{M}}$. As we discuss later, it is important to also include one-body terms in L when s.p. self-energy insertions are taken into account.

It should be emphasized that the normalization condition for the Y-amplitudes is [20])

$$\sum_{\substack{p_1>p_2>k_{\mathrm{F}}\\ \in \mathrm{P}}}|Y_m(p_1p_2,\lambda)|^2-\sum_{\substack{k_{\mathrm{F}}>h_1>h_2\\ \in\mathrm{P}}}|Y_m(h_1h_2,\lambda)|^2=-Z_m^\lambda \tag{3.15}$$

with

$$Z_m^\lambda=\left\{1-\left.\frac{\partial\mu_m(\omega,\lambda)}{\partial\omega}\right|_{\omega=\mu_m(\omega,\lambda)}\right\}^{-1}. \tag{3.16}$$

In the above, p_1 and p_2 are obviously the particle s.p. states within the model space P and h_1 and h_2 are the hole s.p. states within P.

A brief summary of our calculational procedure is in order. The model space reaction matrix $\bar{G}^{\mathrm{M}}$ is calculated from eqs. (3.1) to (3.3). Then we solve the self-consistent equations (3.14) and (3.14a). This may be done by a graphical method where we plot $\mu_m(\omega,\lambda)$ as a function of ω. The self-consistent solution is given by the point where $\omega=\mu_m(\omega,\lambda)$ is satisfied. The slope of the $\mu_m(\omega,\lambda)$ curve at this point is then used in eq. (3.16) to determine the normalization constant Z_m^λ. In this way, we can calculate Y_m and ω_m^-. Using these and $\bar{G}^{\mathrm{M}}$, the energy shift is then calculated using eq. (3.13). Recall that Y_m is the $A\to(A-2)$ transition amplitude defined in eq. (2.12d). If these amplitudes can be determined experimentally, then we can use them directly in eq. (3.13). We don't know how realistic it is to do so, but this seems to be an interesting prospect for further study.

How does the present ring-diagram approach compare with the usual BHF [1,2]) and the model-space BHF (MBHF) approaches [10,13]) for nuclear matter? It may be most convenient to explain this by first examining their diagrammatic structures. As shown in fig. 6, diagram (α) is the typical two-hole-line diagram included in the usual BHF theory. (h_1 and h_2 are hole lines.) Here the box B represents a BHF G-matrix using discontinuous s.p. spectrum, namely a self-consistent spectrum for the hole lines but free-particle spectrum for the particle lines. Diagram (β) is a typical diagram included in the MBHF theory of nuclear matter [10,13]. Here each M-box denotes a model-space reaction matrix $G^{\rm M}$ defined in eq. (3.1) and p_1 to p_4 are all particle lines (with momentum between $k_{\rm M}$ and $k_{\rm F}$), and h_1 and h_2 are hole lines. The main difference between BHF and MBHF is in the treatment of the s.p. spectrum between k_F and k_M (the momentum space boundary of the model space). In BHF, one uses a free particle spectrum in this region, while in MBHF one uses a self-consistent spectrum in this region as we will discuss later. The present calculation goes considerably further. Here we sum up the ring diagrams of the type shown by diagram (γ) of fig. 6 to all orders. Again, each M-box represents a $G^{\rm M}$ vertex whose intermediate states are all particle states outside the model space P. A specific feature is that the intermediate states $i, j, k, \ldots$ to s are all within P and each pair of them, such as the pair (rs), can be either both particles or both holes. Hence the present method sums up the particle–particle ring diagrams of all possible zig-zag shapes to all orders. Clearly the present method sums up a much larger class of diagrams than BHF and MBHF.

It is of interest to note the following feature of eq. (3.13). The expression $\Delta E_0^{\rm pp}$ given by eq. (3.13) reduces to the corresponding expression for the BHF case if we set $k_{\rm M} = k_{\rm F}$ and, in addition, set the Y_m amplitudes equal to their unperturbed values (i.e. in eq. (2.12d) we replace the true wave functions Ψ_m^{A-2} and Ψ_0^A by the respective unperturbed wave functions Φ_m^{A-2} and Φ_0^A). In eq. (3.13), the Y_m amplitudes serve as a kind of distribution function. The effect of the particle-particle ring diagrams is exhibited by the deviation of these amplitudes from their respective unperturbed values. Clearly the magnitudes and distributions of the Y-amplitudes will play an instrumental role in our present calculation.

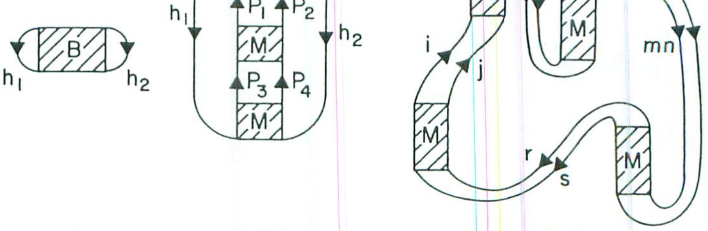

(α) (β) (γ)

Fig. 6. Typical diagrams included in the usual BHF (α), the MBHF (β), and the present ring-diagram (γ) approaches for nuclear matter. Box B denotes a BHF reaction matrix, and box M denotes a model-space reaction matrix of eq. (3.1).

4. Calculation and results

4.1. SINGLE PARTICLE POTENTIAL AND SPECTRUM

An important step in our nuclear matter calculation is the determination of the model-space s.p. potential U. In our formulation described so far, we have used $H=(T+U)+(V-U)\equiv H_0+H_1$, and the s.p. wave functions ϕ_k and energies ε_k are defined by H_0. To carry on the calculation, we must know ϕ_k and ε_k, namely we must know U. For nuclear matter, we use plane waves for ϕ_k and, hence, the quantity to be determined is the s.p. spectrum ε_k.

We adopt a model-space Hartree–Fock method [13]) for determining ε_k. The principle of this method is briefly described below. Using effective interaction theories [21]), one can formally transform the nuclear hamiltonian H into a model-space (P) effective hamiltonian $PH_{\text{eff}}P$, where $H_{\text{eff}}=H_0+PV_{\text{eff}}P$. The effective interaction V_{eff} has in general many-body components such as the one-body part $V_{\text{eff}}^{(1)}$, two-body part $V_{\text{eff}}^{(2)}$, etc. The model-space Hartree–Fock method for determining U is to choose a U such that the condition $PV_{\text{eff}}^{(1)}P=0$ is satisfied. Using a reaction matrix approximation [13]), this condition leads to the following set of self-consistent equations for determining the s.p. spectrum ε_k:

$$\varepsilon_{k_1}=t_{k_1}+\Gamma_{k_1}(\varepsilon_{k_1})\,, \tag{4.1}$$

$$\Gamma_{k_1}(\omega)=2\sum_{h\leq k_F}\langle k_1 h|\bar{G}^{\text{M}}(\omega+\varepsilon_h)|k_1 h\rangle \qquad k_1\leq k_{\text{M}}\,, \tag{4.1a}$$

$$\Gamma_{k_1}(\omega)\equiv 0 \qquad k_1>k_{\text{M}}\,. \tag{4.1b}$$

where t_{k_1} is the s.p. kinetic energy $\hbar^2k_1^2/2m$, $\bar{G}^{\text{M}}$ is the reaction matrix defined in eqs. (3.3) amd (3.1), and k_{M} is $\sim 3\ \text{fm}^{-1}$ which is the momentum space boundary of the model space P. The s.p. potential is the one-body vertex function Γ evaluated at the self-consistent energy $\omega=\varepsilon_{k_1}$, namely

$$U(k_1)=\Gamma_{k_1}(\varepsilon_{k_1})\,. \tag{4.2}$$

A special feature of the above approach for the s.p. potential is that $U(k_1)$ is determined self-consistently for $k_1\leq k_{\text{M}}$, and for $k_1>k_{\text{M}}$ we set $U(k_1)=0$. We will use an effective mass description for the s.p. spectrum. Then the s.p. spectrum is given as

$$\varepsilon_{k_1}=\begin{cases}\dfrac{\hbar^2k_1^2}{2m^*}+\Delta & k_1\leq k_{\text{M}}\\[2ex] \dfrac{\hbar^2k_1^2}{2m} & k_1>k_{\text{M}}\,.\end{cases} \tag{4.3}$$

The effective mass m^* and zero-point energy Δ are determined self-consistently, as described below.

It is convenient to carry out the calculation of eq. (4.1a) in the relative and center-of-mass (RCM) frame. Similarly, we also need to calculate G^{M} of eq. (3.1) in terms of the RCM momentum variables. An essential step in doing so is to replace the projection operator Q^{M} of eq. (3.2) by its angle-average approximation [13]) $\bar{Q}^{\mathrm{M}}$ given by

$$\bar{Q}^{\mathrm{M}}(k, K, k_{\mathrm{F}}, k_{\mathrm{m}}) = \begin{cases} 1 & \text{in regions a, b} \\ 0 & \text{c} \\ [k^2 - k_{\mathrm{F}}^2 + \frac{1}{4}K^2]/kK & \text{d} \\ [(k+\frac{1}{2}K)^2 - k_{\mathrm{M}}^2]/kK & \text{e} \\ [2k^2 - k_{\mathrm{F}}^2 + \frac{1}{2}K^2 - k_{\mathrm{M}}^2]/kK & \text{f}, \end{cases} \tag{4.4}$$

where the values of k and K for the various regions are defined in fig. 7. $\boldsymbol{k}$ and $\boldsymbol{K}$ are related to $\boldsymbol{k}_m$ and $\boldsymbol{k}_n$ by $\boldsymbol{k} = \frac{1}{2}(\boldsymbol{k}_m - \boldsymbol{k}_n)$ and $\boldsymbol{K} = \boldsymbol{k}_m + \boldsymbol{k}_n$. The above result is obtained from eq. (3.2) by assuming that all relative directions between $\boldsymbol{k}$ and $\boldsymbol{K}$ are equally likely and thereby we can average over these directions.

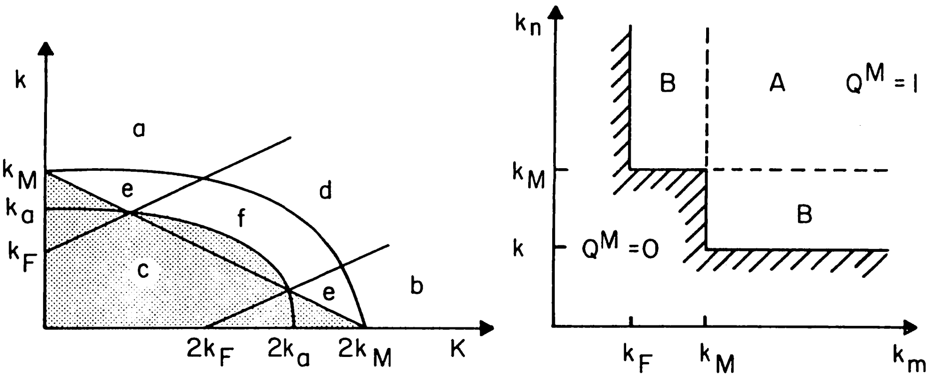

(i) (ii)

Fig. 7. (i) Momentum regions for the angle-averaged projection operator $\bar{Q}^{\mathrm{M}}$ of eq. (4.4). Note that $k_{\mathrm{a}}^2 = \frac{1}{2}(k_{\mathrm{F}}^2 + k_{\mathrm{M}}^2)$ and the two curves are ellipses. (ii) The projection operator Q^{M} of eq. (3.2).

Using the above averaged $\bar{Q}^{\mathrm{M}}$, eq. (3.1) for the model space reaction matrix can be decomposed into separate partial wave channels. Namely for each partial wave channel α such as the ${}^3\mathrm{S}_1$-${}^3\mathrm{D}_1$ channel, we have

$$\langle kl|G^{\mathrm{M}}(\omega, K\alpha)|k'l'\rangle = \langle kl|V|k'l'\rangle + \frac{2}{\pi}\int_0^\infty k''^2\,\mathrm{d}k'' \sum_{l''} \frac{\langle kl|V|k''l''\rangle \bar{Q}^{\mathrm{M}}(k'', K, k_{\mathrm{F}}, k_{\mathrm{M}}) \langle k''l''|G^{\mathrm{M}}(\omega, K\alpha)|k'l'\rangle}{\omega - H_0(k''K)}, \tag{4.5}$$

where α stands for the partial wave quantum numbers $(ll'SJT)$, and K the center-of-mass momentum. For simplicity, the K and (SJT) quantum numbers associated with the bra and ket vectors have been suppressed. For example, $\langle kl|$ should in fact be $\langle klSJT, K|$. $H_0(k'', K)$ is the unperturbed energy of the intermediate state (k'', K);

and its determination is discussed later. We note that our convention for plane waves is

$$\langle r|klSJ\rangle = j_l(kr)\mathscr{Y}_{lSJ}(\hat{r}) \tag{4.6}$$

where $j_l(kr)$ is the spherical Bessel function, and $\mathscr{Y}$ is the vector spherical harmonics corresponding to $\boldsymbol{l}+\boldsymbol{S}=\boldsymbol{J}$. We also note that G^{M} is diagonal in K and α, as indicated by eq. (4.5). This is a consequence of using the angle averaged projection operator $\bar{Q}^{\mathrm{M}}$ of eq. (4.4).

Angle-average approximations [22]) are also used in eqs. (4.2) and (4.1a). This leads to the familiar equation for the s.p. potential; e.g. we have for $k_1 < k_{\mathrm{F}}$

$$U(k_1) = \sum_{\alpha} (2T+1)(2J+1)\left\{\frac{8}{\pi}\int_0^{k_-} k^2\,\mathrm{d}k\, G^{\mathrm{M}}_{lSJT}(k, \bar{K}_1) + \frac{1}{\pi k_1}\int_{k_-}^{k_+} k\,\mathrm{d}k[k_{\mathrm{F}}^2 - k_1^2 + 4k(k_1-k)]G^{\mathrm{M}}_{lSJT}(k, \bar{K}_2)\right\}, \tag{4.7}$$

where

$$\begin{aligned} k_- &= \tfrac{1}{2}(k_{\mathrm{F}} - k_1) \\ k_+ &= \tfrac{1}{2}(k_{\mathrm{F}} + k_1) \\ \bar{K}_1^2 &= 4(k_1^2 + k^2) \\ \bar{K}_2^2 &= 4(k_1^2 + k^2) - (2k + k_1 - k_{\mathrm{F}})(2k + k_1 + k_{\mathrm{F}}) \end{aligned} \tag{4.7a}$$

and the partial wave G^{M} matrix elements are given by

$$G^{\mathrm{M}}_{lSJT}(k, K) \equiv \langle kl|G^{\mathrm{M}}(\omega, K\alpha)|kl\rangle \tag{4.7b}$$

with

$$\omega = \frac{\hbar^2 k^2}{m^*} + \frac{\hbar^2 K^2}{4m^*} + 2\Delta\,. \tag{4.7c}$$

In the above, we have used the effective mass description for the s.p. spectrum as given by eq. (4.3). Now we return to the intermediate-state spectrum $H_0(k'', K)$ of eq. (4.5). Referring to fig. 7(ii), the momentum variables k_m and k_n corresponding to k'' and K may be in either region A or B. In region A, both particles have momentum $>k_{\mathrm{M}}$. Then according to eq. (4.3) we have for this region

$$H_0(k'', K) = \frac{\hbar^2 k''^2}{m} + \frac{\hbar^2 K^2}{4m}\,. \tag{4.8}$$

But in regions B, we have one nucleon with momentum $>k_{\mathrm{M}}$ while the other with

Based on this, we have made our choice of k_M as stated above. Note that our choice of K_M is different from theirs: we use a fixed k_M irrespective of the k_F values while their k_M varies with k_F. It is difficult to assess precisely which of these two schemes is better. For $k_F \approx 1.5\ \mathrm{fm}^{-1}$, those two choices are clearly very similar to each other. In the regions of very large and very small k_F, we feel that our choice is more reasonable. For example, if $k_F = 0.5\ \mathrm{fm}^{-1}$ then $k_M = 2k_F = 1.0\ \mathrm{fm}^{-1}$ would certainly seem to be too small.] In fig. 9 we show a s.p. spectrum calculated from the Reid NN interaction [17]). Clearly it is rather similar to the spectrum calculated using the Paris NN interaction; the Paris spectrum being a few MeV lower. We note that the numerical values of our model-space s.p. spectrum are in fact quite close to those of the continuous s.p. spectrum of Mahaux and his collaborators [3]), although these two spectra employ different methods of derivation.

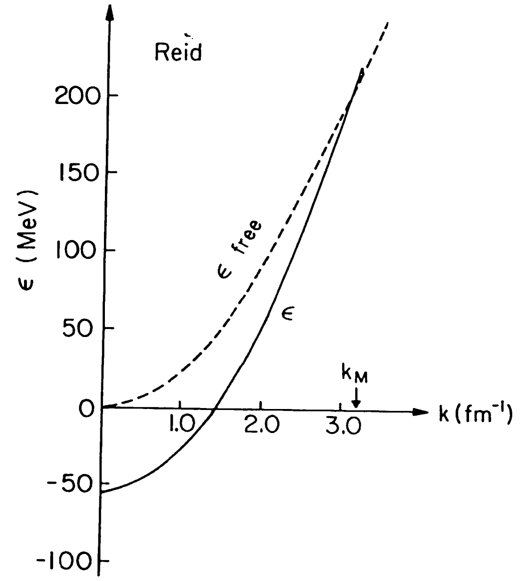

Fig. 9. Same as fig. 8 except for the Reid NN interaction.

Remember that we have used an effective mass description for the s.p. spectrum as shown in eq. (4.3). In table 1, we give our results for the effective mass m^* and the zero-point energy Δ for various k_F values and for both the Paris and Reid NN interactions. When plotted as a function of k_F, they form rather smooth curves. It should be pointed out that it is often not very accurate to fit our calculated spectrum by a parabola with two parameters m^* and Δ. (We have used a six point fit for the momentum range 0 to k_M, three points below k_F and three above. Typical differences between calculated and fitted spectra are ~1-2 MeV. In order to carry out calculations in the RCM coordinates, it is however necessary to use the m^* and Δ description for the s.p. spectrum.) As shown in the table, values of m^* calculated from the two NN potentials are quite similar to each other, but there are considerable differences between the two sets of Δ values. To see the trend of the dependence of m^* and Δ

TABLE 1

Self-consistent effective mass m^* and zero-point energy Δ for various k_F values, calculated with $k_M = 3.2\ \mathrm{fm}^{-1}$ and the Paris and Reid NN interactions

	$k_F(\mathrm{fm}^{-1})$	m/m^*	Δ (MeV)
Paris	1.20	1.190	−44.55
	1.30	1.234	−53.77
	1.36	1.262	−59.66
	1.40	1.275	−63.50
	1.50	1.327	−73.71
	1.60	1.375	−84.23
	1.70	1.435	−95.22
	1.80	1.504	−106.28
Reid	1.00	1.120	−24.51
	1.10	1.155	−31.09
	1.20	1.196	−38.42
	1.30	1.244	−46.22
	1.36	1.275	−51.06
	1.40	1.289	−54.20
	1.50	1.347	−62.45
	1.60	1.402	−70.43

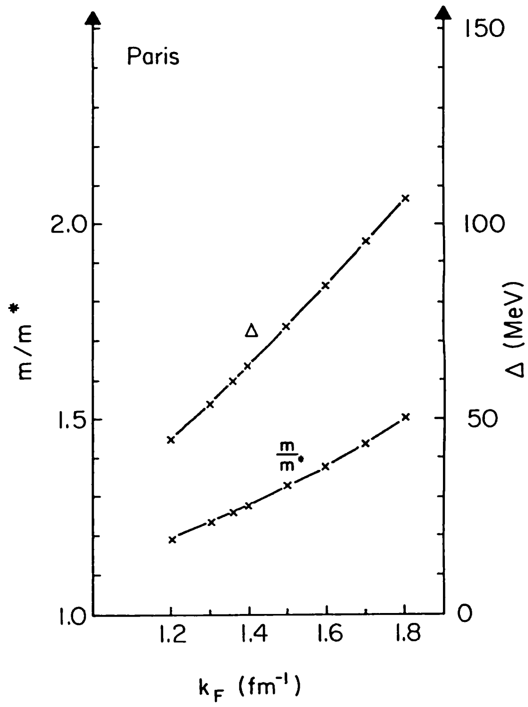

Fig. 10. Dependence of m^*, and Δ on k_F. Calculations were made with the Paris NN potential an
$k_M = 3.2\ \mathrm{fm}^{-1}$.

on the values of k_F, we plot our results for them in fig. 10 for the Paris potential. The corresponding curves for the Reid potential are rather similar.

4.2. ANGLE-AVERAGE APPROXIMATION FOR RPA EQUATION

We now turn to the calculation of the energy shift ΔE_0^{pp} of eq. (3.13). To do so, we need to know the transition amplitudes Y and the model-space reaction matrix $\bar{G}^M$. We have just described how to calculate $\bar{G}^M$ in the previous sub-section. Now we discuss how to calculate the transition amplitudes Y from the RPA-type secular equation (3.14).

As it stands, eq. (3.14) is not convenient for computation. It is expressed in terms of the laboratory momentum variables; its indices $(i, j. e, f)$ are in fact the laboratory s.p. momenta $(\boldsymbol{k}_i, \boldsymbol{k}_j, \boldsymbol{k}_e, \boldsymbol{k}_f)$. Our plan is to use a momentum-space discretization method [22-24]) to convert eq. (3.14) into a finite dimensional matrix equation. To do this in terms of these laboratory momentum variables will lead to matrix equations of impractically large dimensions. It may become greatly simplified if we can transform this equation to its RCM representation. For the calculation of $\bar{G}^M$, we have already used the angle-average approximation as discussed in sect. 4.1. Hence $\bar{G}^M$ is diagonal in its center-of-mass momentum variable. This simplifies eq. (3.14) slightly but is still not adequate. It seems to be indispensable that we also have to make an angle-average approximation for the occupation factor $(\bar{n}_i\bar{n}_j - n_i n_j) = 1 - (n_i + n_j)$ of eq. (3.14).

We define a function $Q_R(\boldsymbol{k}_i, \boldsymbol{k}_j) = 1 - (n_i + n_j) = 1$ or -1 depending on the values of k_i and k_j. This is seen clearly in fig. 11(i) where Q_R is equal to 1 in regions A and B (i and j are both particles) and -1 in region C (i and j are both holes). Q_R is equal to zero for all other regions. The values of $Q_R(k, \boldsymbol{K})$ clearly depends on

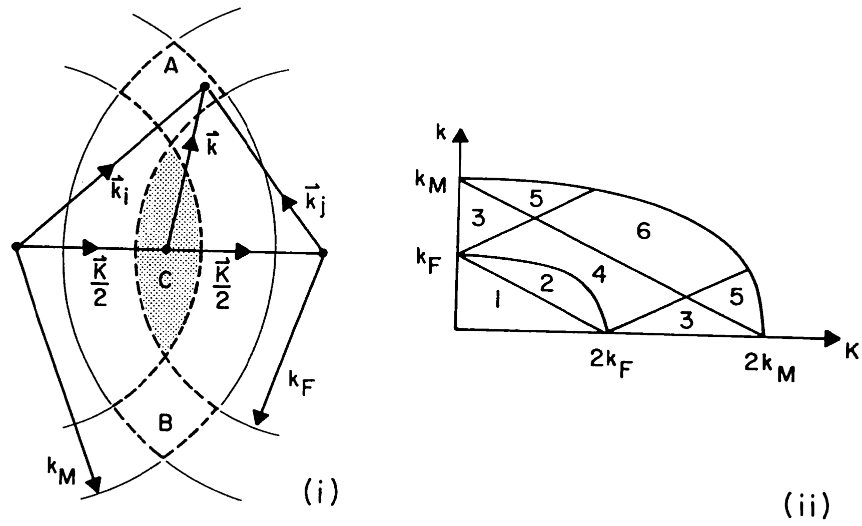

Fig. 11. Regions for the occupation factor $Q(\boldsymbol{k}_i, \boldsymbol{k}_j) = 1 - n_i - n_j$ and its angle-average approximation $\bar{Q}_R(k, K, k_F, k_M)$. In (ii) the lines are $(k - \frac{1}{2}K) = \pm k_F$ and $k + \frac{1}{2}K = k_F$ and k_M. The curves are ellipses.

the angle between $\boldsymbol{k}$ and $\boldsymbol{K}$. Assuming that all values for this angle are equally likely, we can replace $Q_R(\boldsymbol{k}, \boldsymbol{K})$ by its angle-average approximation $\bar{Q}_R(k, K, k_F, k_M)$. With the help of fig. 11(i), the values of $\bar{Q}_R$ are obtained as

$$\bar{Q}_R(k, K, k_F, k_M) = \begin{cases} -1 & \text{region } 1 \\ -|x_1| & 2 \\ 1 & 3 \\ |x_1| & 4 \\ |x_2| & 5 \\ \min(|x_1|, |x_2|) & 6 \end{cases} \tag{4.9}$$

where

$$x_1 \equiv (k_F^2 - k^2 - \tfrac{1}{4}K^2)/kK,$$
$$x_2 \equiv (k_M^2 - k^2 - \tfrac{1}{4}K^2)/kK. \tag{4.9a}$$

The regions 1 to 6 of eq. (4.9) refer to the regions in the (k, K) plane shown in fig. 11(ii).

The replacement of Q_R by its angle-average approximation $\bar{Q}_R$ greatly simplifies eq. (3.14); it can now be decomposed into separate partial-wave equations. Namely, it becomes for partial wave channel α

$$\sum_{l'} \int \mathrm{d}k' \left\{ \varepsilon_{kK} \delta(k-k') \delta_{ll'} + \lambda \frac{2k'^2}{\pi} \bar{Q}_R(k, k) \langle kl | L(\omega, K) | k'l' \rangle \right\} Y_m(k'l'k, \lambda)$$
$$= \mu_m(\omega, \lambda) Y_m(klK, \lambda), \tag{4.10}$$

where $\bar{Q}_R(k, K)$ is an abbreviation for $\bar{Q}_R(k, K, k_F, k_M)$ of eq. (4.9). ε_{kK} is the unperturbed energy $\hbar^2k^2/m^* + \hbar^2K^2/4m^* + 2\Delta$. The wave function (kl) stands for the RCM partial wave function $(klSJT, K)$ and similarly for (k', l'), as explained in sect. 4.1. Clearly, eq. (4.10) is to be solved together with the self-consistent condition (3.14a), giving the self-consistent solution $\omega_m^-(\lambda)$. We emphasize that eq. (4.10) is much simpler for calculation than eq. (3.14), and this is made possible by the introduction of the angle-average approximation for $1-(n_i+n_j)$. This enables us to solve eq. (3.14) separately for each partial wave channels, such as the $^3S_1$-$^3D_1$ channel. It should be pointed out that this approximation is quire similar to the angle-average approximations for the Pauli exclusion operators and potential energy calculations which have been used in almost all existing nuclear matter calculations.[1-4,22,25])

We now turn to the vertex function $L(\omega, K)$ of eq. (4.10), which is a standard equation for determining the poles and residues of the particle–particle Green functions[19,20]). L is the irreducible vertex function which has, in general, both two-body and one-body terms. For simplicity, we included in eq. (3.14b) only a two-body term, $\bar{G}^M$, in L. The following consideration is important. As shown by eqs. (3.15) and (3.16), the normalization constant Z_m for the Y_m amplitudes depend on the energy derivatives of the self-consistent energy μ_m. Hence, Z_m in fact depends on the energy derivative $dL/d\omega$. As described in sect. 4.1, we have introduced a s.p. potential U defined by the self-energy vertex function Γ (see eqs. (4.1) to (4.2)). Thus the one-body vertex functions have already entered our calculations. Therefore our L is in fact

$$\langle ij|L(\omega)|ef\rangle = \bar{G}^{\mathrm{M}}_{ijef} + \delta_{ie}\delta_{jf}\{S_i(\omega_1) + S_j(\omega_2)\} \tag{4.11}$$

with the one-body vertex function given as

$$S_i(\omega_1) \equiv \Gamma_i(\omega_1) - U(i) \tag{4.11a}$$

and similarly for $S_j(\omega_2)$. It is readily seen that $\omega_1 = \omega - \varepsilon_j$ and $\omega_2 = \omega - \varepsilon_i$. For clarity, the above equations are expressed in the laboratory frame where the indices $i, j, \dots$ stand for the laboratory momenta $k_i, k_j, \dots$. Note that our choice of U, as discussed in sect. 4.1, is to make $S_i(\omega = \varepsilon_i) = 0$ (and $S_j(\omega = \varepsilon_j) = 0$). This certainly does *not* imply at all that $S_i(\omega_1) = S_j(\omega_2) = 0$ and $dS_i(\omega_1)/d\omega = dS_j(\omega_2)/d\omega = 0$. In fact these energy derivatives will be rather large and will play an important role in determining Z_m. With $L(\omega)$ given by eq. (4.11), the ring diagrams included in our nuclear matter calculations are in fact of the general structure shown in fig. 12.

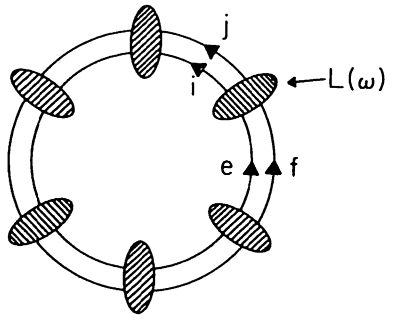

Fig. 12. A general sign diagram included in our nuclear matter calculations. The vertex function $L(\omega)$ is given by eq. (4.11).

As discussed earlier, in our calculations we need the RCM matrix elements $\langle kl|L(\omega, K)|k'l'\rangle$. For given RCM momenta k and K, the angle-averaged values for k_i^2 and k_j^2 being both particles (regions A and B of fig. 11(i)) or both holes (region C of fig. 11(i)) can be readily found. Namely both are given by $(k^2 + \frac{1}{4}K^2)$. It has been necessary at several stages of our calculations to use the angle-average approximations. The same is also true for treating S_i and S_j of eq. (4.11). Thus the matrix element of $L(\omega, K)$ of eq. (4.10) is obtained as

$$\langle kl|L(\omega, K)|k'l'\rangle = \langle kl|\bar{G}^{\mathrm{M}}(\omega, K\alpha)|k'l'\rangle + 2\delta_{kk'}\delta_{ll'}\{\Gamma_{\bar{k}_1}(\omega - \varepsilon_{\bar{k}_1}) - U(\bar{k}_1)\}\,, \tag{4.12}$$

where $\bar{G}^{\mathrm{M}}$ has been given by eq. (3.3), and Γ and U have been given by eqs. (4.1) to (4.2). Recall that $\bar{k}_1^2 = k^2 + \frac{1}{4}K^2$.

We now proceed to solve eqs. (4.10) and (4.12). First, we recall that they are t be solved together with the self-consistent condition (3.14a), i.e. $\mu_m(\omega, \lambda) = \omega \equiv$ $\omega_m^-(\lambda)$. It is certainly numerically possible to carry out such self-consistent solution by way of graphical methods. In so doing, one needs a rather large amount o computer time. It is more convenient, as well as physically more meaningful, t carry out the following perturbative solution. We have found that the dependenc of $\bar{G}^{\mathrm{M}}$ on ω is quite weak for ω in the vicinity of ω_m^-. (Note that only ω_m^- and th corresponding Y_m amplitudes enter in our calculation of ΔE_0^{pp}, as shown by eq (3.13).) Thus the dependence of $L(\omega, K)$ on ω comes almost entirely from that o $\Gamma_{\bar{k}_1}(\omega)$. As is well known, $-\mathrm{d}\Gamma/\mathrm{d}\omega$ is closely related to the two-body wound integra $\kappa^{(2)}$ whose values are ~0.10.

Let us first calculate $\mathrm{d}\Gamma/\mathrm{d}\omega$. From eqs. (4.1a) and (3.1) we have

$$\frac{\mathrm{d}}{\mathrm{d}\omega}\Gamma_{k_1}(\omega) = -\frac{2}{A}\sum_{k_h \leq k_\mathrm{F}} \langle k_1 k_h | \bar{G}^{\mathrm{M}} \left(\frac{Q^{\mathrm{M}}}{e}\right)^2 \bar{G}^{\mathrm{M}} | k_1 k_h \rangle\,, \qquad (4.1$$

where $\bar{G}^{\mathrm{M}}$ and e are both dependent on ω, i.e. $\bar{G}^{\mathrm{M}} = \bar{G}^{\mathrm{M}}(\omega + \varepsilon_h)$ and e $(\omega + \varepsilon_h) - H_0$ (see eqs. (4.8) and (4.8a) for H_0). At the self-consistent energy $\omega = \varepsilon$ we have $k^{(2)}(k_1) = -(\mathrm{d}/\mathrm{d}\omega)\Gamma_{k_1}(\omega)$ which is the familiar two-body wound integra Using angle average approximations quite similar to those used for the derivatio of $U(k_1)$ of eq. (4.7), we obtain from eq. (4.13)

$$\begin{aligned}
\kappa^{(2)}(k_1, \omega) &\equiv -\frac{\mathrm{d}}{\mathrm{d}\omega}\Gamma_{k_1}(\omega) \\
&= \frac{8}{\pi}\sum_{\alpha}(2T+1)(2J+1)\int_0^{k_-} k^2\,\mathrm{d}k \langle k\alpha | G\left(\frac{Q}{e}\right)^2 G(\bar{K}_1) | k\alpha \rangle \\
&\quad + \frac{1}{2\pi k_1}\sum_{\alpha}(2T+1)(2J+1) \\
&\quad \times \int_{k_-}^{k_+} \mathrm{d}k[k_\mathrm{F}^2 - k_1^2 + 4k(k_1 - k)]k\langle k\alpha | G\left(\frac{Q}{e}\right)^2 G(\bar{K}_2) | k\alpha \rangle\,, \qquad (4.1
\end{aligned}$$

where $k_\pm$, $\bar{K}_1$ and $\bar{K}_2$ have been given in eq. (4.7a). The matrix elements $G(Q/e)^2 G(K)$ are abbreviations for

$$\langle k\alpha | G\left(\frac{Q}{e}\right)^2 G(k) | k\alpha \rangle \equiv \sum_{l'}\frac{2}{\pi}\int_0^{\infty} k'^2\,\mathrm{d}k' \left\{\frac{\bar{Q}^{\mathrm{M}}(k', K)\langle k'l' | G^{\mathrm{M}}(\omega, k\alpha) | kl \rangle}{\omega - H_0(k', K)}\right\}^2, \qquad (4.$$

where $\bar{Q}^{\rm M}$ is the $\bar{Q}^{\rm M}(k, K, k_{\rm F}, k_{\rm M})$ of eq. (4.4) and H_0 has been given by eqs. (4.8) and (4.8a). Recall that α stands for the quantum numbers $(ll'SJT)$ and (kl) represents $(klSJT, K)$.

In fig. 13, we present some representative values of $\kappa^{(2)}(k_1, \omega)$. As shown, they are generally rather small. (This is mainly because we have used a model space with $k_{\rm M} = 3.2\ {\rm fm}^{-1}$.) We have found that $\kappa^{(2)}$ generally varies rather slowly with ω and k_1 in the energy and momentum regions important for our present calculation. Consequently, $d\Gamma/d\omega$ has the same behavior and it should be a good approximation to solve eqs. (4.10), (4.12) and (3.14) with their ω-dependent terms treated by first order perturbation theory[*], as is done in the present calculation.

4.3. NUCLEAR MATTER BINDING ENERGIES

Having calculated the reaction matrix $\bar{G}^{\rm M}$ and the transition amplitudes Y in the previous two subsections, we are now ready to calculate the energy shift $\Delta E_0^{\rm pp}$ of eq. (3.13). Using angle-average approximations similar to those used in the derivation of eqs. (4.4) and (4.9), we can express $\Delta E_0^{\rm pp}$ as

$$\begin{aligned}\frac{\Delta E_0^{\rm pp}}{A} = \frac{3}{\pi^2 k_F^3} \sum_\alpha (2J+1)(2T+1) \int_0^1 d\lambda \int_0^{2k_{\rm M}} K^2\, dK \sum_m \sum_{ll'} \\ \times \int_0^{k_{\rm M}} k^2\, dk \int_0^{k_{\rm M}} k'^2\, dk' \\ \times Y_m(klK, \lambda)^* \langle kl | G^M(\omega_m^-(\lambda), K\alpha) | k'l' \rangle Y_m(k'l'K, \lambda)\,, \qquad (4.16)\end{aligned}$$

which is the potential energy per nucleon (PE/A) of nuclear matter. Let us briefly

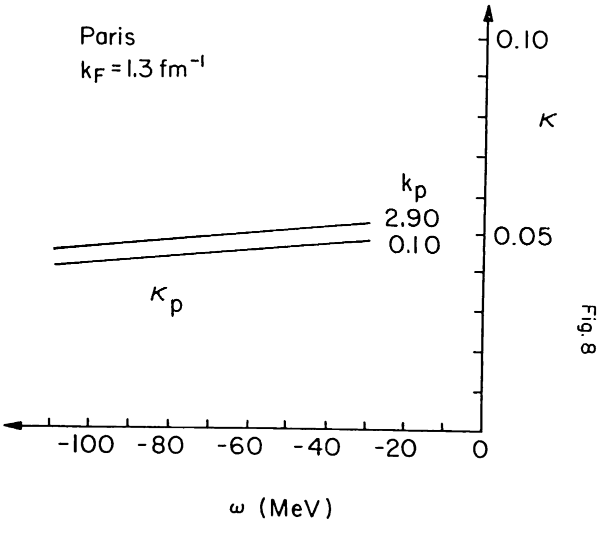

Fig. 13. Variation of $\kappa^{(2)}(k_1, \omega)$ with k_1 and ω, calculated with $k_{\rm F} = 1.3\ {\rm fm}^{-1}$ and the Paris NN interaction. $k_{\rm M} = 3.2\ {\rm fm}^{-1}$ is used.

---

[*] Briefly speaking, we consider $[H_0 + A(\omega)]\psi(\omega) = E(\omega)\psi(\omega)$ with $\omega = E(\omega)$. H_0 is ω-independent. We first solve $[H_0 + A(\omega_0)]\phi_0 = E_0\phi_0$, and then treat $(\omega - \omega_0)\, dA/d\omega$ by first order perturbation theory (for ω not very far away from ω_0.) This gives, for example, $E(\omega) \approx E_0 + (\omega - \omega_0)\langle\bar{\phi}_0|\, dA/d\omega\, |\phi_0\rangle$.

explain the above. α denotes the partial wave quantum numbers ($ll'SJT$). For each α, λ and K we solve the secular equation (4.10) to obtain $\omega_m^-(\lambda)$ and $Y_m(\ldots,\lambda)$. Recall that, as shown by eq. (3.13), ΔE_0^{pp} was originally expressed in terms of the laboratory frame momentum variables $(\boldsymbol{k}_i, \boldsymbol{k}_j)$ and $(\boldsymbol{k}_k, \boldsymbol{k}_l)$. We have now transformed it to the RCM frame with momentum variables k, k' and K. This is made possible by replacing the occupation factor $(\bar{n}_i\bar{n}_j - n_i n_j)$ by its angle-average approximation $\bar{Q}_{\text{R}}$ of eq. (4.9) in the derivation of the RPA type seculation equation (4.10). Thus the amplitudes Y's are already angle averaged, and therefore in eq. (4.16) the upper integration limits for k and K are respectively k_{M} and $2k_{\text{M}}$. We note that the Y's are normalized to Z_m^λ according to eq. (3.15) which is expressed in terms of the laboratory momentum variables. In actual calculations this equation is transformed into the RCM frame also with the approximation that the occupation factor $(\bar{n}_i\bar{n}_j - n_i n_j)$ is replaced by its angle average $\bar{Q}_{\text{R}}$. Clearly, the binding energy per nucleon (BE/A) is given by $-\text{BE}/A = 3\hbar^2 k_{\text{F}}^2/10m + \Delta E_0^{\text{pp}}/A$.

The integrations in eq. (4.16) are carried out numerically using gaussian mesh points and weights. We have found that satisfactory accuracy is obtained when using approximately (3, 3, 30) mesh points for the (λ, K, k) integrations, respectively. It is interesting to note that when setting $\lambda = 1$ (i.e. $\int_0^1 \mathrm{d}\lambda$ is removed), $k_{\text{M}} = k_{\text{F}}$, and $L = 0$ in eq. (4.10), eq. (4.16) becomes the usual BHF formula for calculating PE/A. We have used this limit for performing BHF nuclear matter calculations and obtained results in very good agreement with results of other BHF calculations*. This serves as a check of our computer programs. Note that when L is set to 0 in eq. (4.10), the amplitudes Y_m reduce to their respective unperturbed values (i.e. the true wave functions Ψ_m^{A-2} and Ψ_0^A in eq. (2.12d) are replaced by the respective unperturbed wave functions Φ_m^{A-2} and Φ_0^A).

In figs. 14 and 15 we show the results of our nuclear matter BE/A calculations as a function of k_{F} (or density $\rho = 2k_{\text{F}}^3/3\pi^2$) for both the Paris and the Reid NN interactions. The curves labelled RING are our ring diagram calculations outlined by eq. (4.16). The results from BHF calculations, labelled BHF, are also given for comparison. Let us discuss fig. 14 first. Clearly, the RING calculations give an additional binding energy of about 4 MeV per nucleon, as compared with the BHF result. This gain in binding energy is perhaps attributable, to a large extent, to the use of a "continuous" s.p. spectrum which has an attractive potential energy in the momentum region k_{F} to k_{M}. Ma *et al.* [10,13]) have carried out model-space BHF (MBHF) nuclear matter calculations which are essentially BHF calculations using a "continuous" s.p. spectrum for momentum $k \leq k_{\text{M}}$. They have found that MBHF nuclear matter calculations using the Paris NN interaction gives an additional BE/A of about 4 MeV compared with the corresponding BHF calculations. Lejeune, Mattzolff and Grange [27]) have performed BHF nuclear matter calculations using the Paris NN interactions and a continuous s.p. spectrum. Their results and those of Ma *et al.* are in fact in very good agreement with each other; their calculations

---

* We have compared our BHF results with those of refs. [10,13]) using the Paris and Reid potentials, of ref. [22]) using the Reid potential, and of Day and Wiringa's calculation [26]) using the Paris potential.

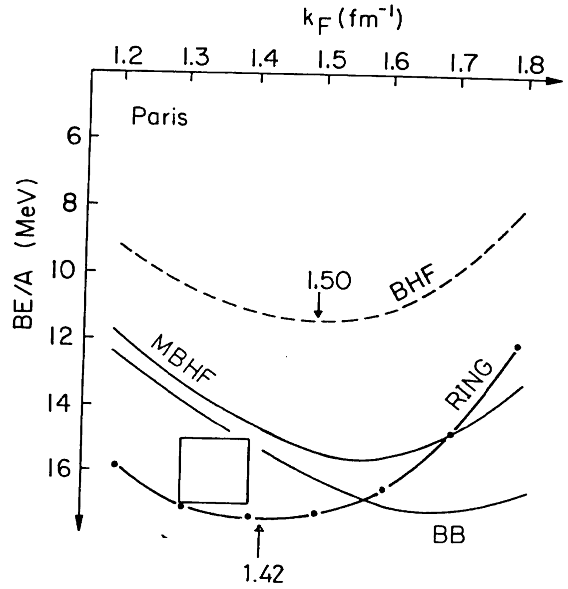

Fig. 14. Results of ring diagram nuclear matter calculations (RING) obtained with eq. (4.16), $k_M = 3.2\,\text{fm}^{-1}$, and the Paris NN interaction. Results for the BHF calculations are also shown (BHF). The arrows indicate the saturation Fermi momenta. The box indicates the empirical nuclear matter properties. The curves labelled BB and MBHF are respectively Day and Wiringa's [26]) and Kuo, Ma and Vinh Mau's [10]) results. See text for further explanation.

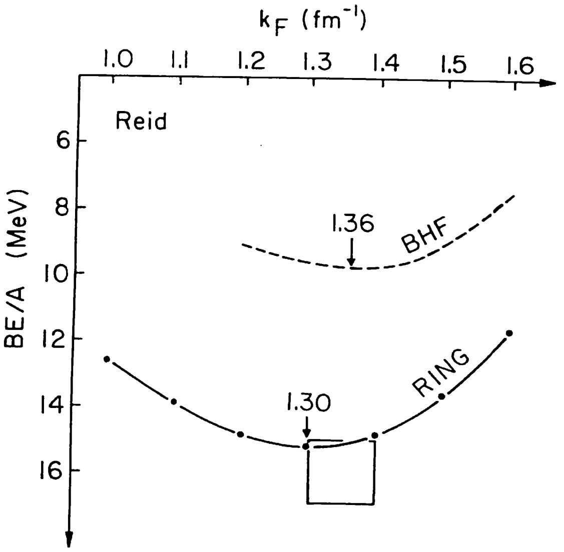

Fig. 15. Same as fig. 14 except for the Reid NN interaction.

using a continuous s.p. spectrum give an additional BE/A of about 4 MeV compared with those using a conventional discontinuous s.p. spectrum. Similar calculations have also been carried out by Dey and Matin [28]). They have, however, found that the gain in BE/A due to the use of a continuous s.p. spectrum is about 7 MeV. All these calculations indicate that the use of "continuous" s.p. spectrum of the form shown in fig. 8 is very likely to give an extra BE/A of several MeV compared with the case of using a conventional discontinuous BHF s.p. spectrum.

Day and Wiringa [26]) have performed both variational and Brueckner–Bethe calculations of nuclear matter using the Paris potential. The latter included two-, three- and four-hole line contributions. They have found that the results given by these two approaches generally agree with each other rather well. In fig. 14, we include their Brueckner–Bethe result (labelled BB) for comparison. As shown, their binding energy agrees with our RING result rather well, but their saturation density is significantly higher. Kuo, Ma and Vinh Mau [10]) have performed model-space Brueckner Hartree-Fock calculations of nuclear matter using the Paris potential. Their results (labelled MBHF) are also included in fig. 14 for comparison.

The most interesting feature of fig. 14 is therefore not that our RING calculations give satisfactory BE/A. It is, instead, that they give rather satisfactory saturation density. Most likely, this is due to the inclusion of the particle–particle ring diagrams to all orders in our calculations. Let us trace our calculations. The potential energy per nucleon of our calculations is evaluated according to eq. (4.16). Let us decompose $\Delta E_0^{\mathrm{pp}}/A$ of this equation into its λ-integrands for each partial waves:

$$\frac{\Delta E_0^{\mathrm{pp}}}{A}=\sum_{\alpha}\Delta E_{\alpha}=\sum_{\alpha}\int_0^1 \mathrm{d}\lambda\, I_{\alpha}(\lambda)\,. \tag{4.17}$$

We show in table 2 a set of typical values for $I_{\alpha}(\lambda)$ and ΔE_{α}. For most partial wave channels, $I_{\alpha}(\lambda)$ does not vary much from $\lambda=0$ to $\lambda=1$. But for the ^{3}S$_1$-^{3}D$_1$ channel, we notice that there is a large change of $I_{\alpha}(\lambda)$; it changes from -12.7 to -29.9 when λ changes from ~0.11 to ~0.89. It is easily seen that $\lambda=0$ corresponds to the case in which only terms of first order in $\bar{G}^{\mathrm{M}}$ are included in ΔE_0^{pp} of eq. (4.16). Hence we have the rather interesting and important observation that it is the ^{3}S$_1$-^{3}D$_1$ channel where the effect of ring diagrams is most pronounced. Since it is this channel where the NN tensor interaction is most important, it may be inferred from our calculations that the importance of the ring diagram correlations is closely related to the NN tensor interaction.

Fig. 14 seems to indicate that the effect of the ring diagrams is rather sensitive to the nuclear matter density. Let us use the BHF curve as a reference. With respect to it, we see that the ring diagrams give a considerably larger gain in BE/A for low density than for high density. Thus the inclusion of the ring diagrams shifts the saturation to a lower value ($k_{\mathrm{F}}\cong 1.4\ \mathrm{fm}^{-1}$ as shown by the figure). Let us investigate this point more closely.

In fig. 16 we show the contributions to PE/A from the ^{3}S$_1$-^{3}D$_1$ partial wave channels for various k_{F} values. For the Paris NN interaction, the ring diagram calculations are represented by curves 1 and the BHF calculation by curves 2. For the Reid NN interaction, the former are represented by curves 3 and the latter by

TABLE 2

A decomposition of $\Delta E^{\mathrm{pp}}/A$ of eq. (4.16)

α	0.1127	0.5000	0.8873	$\int_0^1 \mathrm{d}\lambda \ldots$
$^1S_0$	−16.762	−16.974	−17.212	−16.981
$^3S_1$-$^3D_1$	−12.719	−20.708	−29.867	−21.033
$^1P_1$	4.922	4.543	4.229	4.562
$^3P_0$	−3.767	−3.749	−3.726	−3.748
$^3P_1$	11.972	10.726	9.755	10.802
$^3P_2$-$^3F_2$	−8.527	−8.980	−9.491	−8.996
$^1D_2$	−3.187	−3.133	−3.085	−3.135
$^3D_2$	−4.607	−4602	−4.632	−4.612
$^3D_3$-$^3G_3$	0.483	0.287	0.102	0.290
$^1F_3$	0.980	0.949	0.920	0.950
$^3F_3$	1.857	1.801	1.748	1.802
$^3F_4$-$^3H_4$	−0.625	−0.622	−0.618	−0.622
$^1G_4$	−0.567	−0.552	−0.538	−0.553
$^3G_4$	−0.878	−0.858	−0.839	−0.858
$^3G_5$-$^3I_5$	0.143	0.134	0.125	0.134
$L > 4$				0.309
PE/A				−41.688
KE/A				24.384
BE/A				−17.304

curves 4. Consider the $^3S_1$-$^3D_1$ channel first, and we note that in this channel the NN tensor interaction plays an important role. It is well known that the intermediate states induced by the NN tensor interaction are mainly of moderately high excitation energy (~300 MeV) [ref. ^{29})]. At high densities, these intermediate states are to a large extent blocked (because k_F is large). At lower densities, these states are relatively empty. Thus if the ring diagrams are induced mainly by the NN tensor interaction, then we expect their effect to be more pronounced at low densities than at high densities. This conjecture is clearly supported by our results, as shown by the $^3S_1$-$^3D_1$ curves of fig. 16. Here curves 1 and 2 are rather close to each other at $k_F \sim 1.6\,\mathrm{fm}^{-1}$, but at $k_F \sim 1.2\,\mathrm{fm}^{-1}$ curve 1 becomes considerably lower. Similar behavior is also observed for curves 3 and 4.

Turning to the $^1S_0$ curves of fig. 16, we see that curves (1, 3) are respectively higher than curves (2, 4) in the region of high densities. This suggests that the effect of the short-range repulsion of the NN interaction is also enhanced by the ring diagrams. (This enhancement is also evident for the $^3S_1$-$^3D_1$ curves of fig. 16.) That the difference between curves 3 and 4 is larger than the difference between 1 and 2 is perhaps a reflection that the Reid NN interaction has a stronger short-range repulsion than the Paris NN interaction.

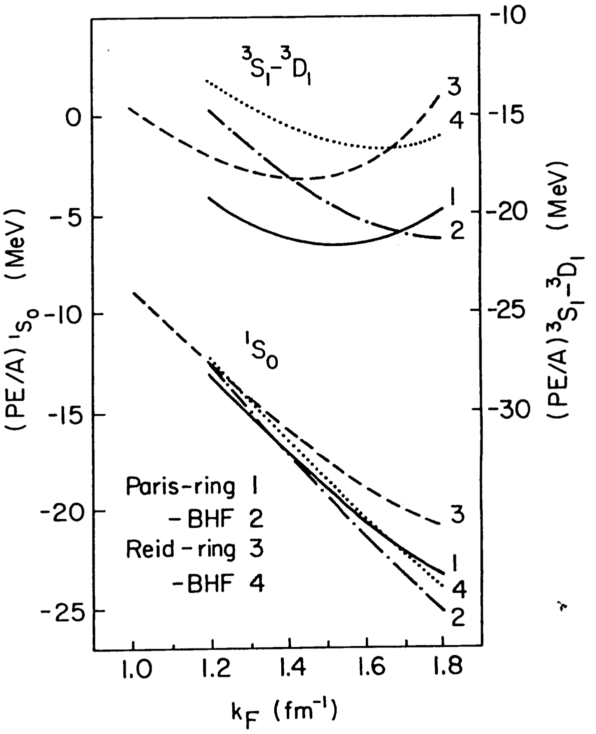

Fig. 16. Contributions to the potential energy per nucleon (PE/A) from the $^1S_0$ and $^3S_1$-$^3D_1$ channels, for the Paris and Reid NN interactions. Calculations including ring diagrams are denoted by "RING", and the BHF calculations are denoted by "BHF".

Let us now go back to fig. 15 where nuclear matter saturation curves calculated with the Reid NN interaction are shown. The BHF calculation gives BE/$A \sim 9.5$ MeV with a saturation Fermi momentum $k_F \sim 1.36\ \mathrm{fm}^{-1}$. Just like the case with the Paris NN interaction of fig. 14, the ring diagrams shift the saturation density to a much lower value ($k_F \sim 1.30\ \mathrm{fm}^{-1}$). It is interesting to note that this k_F is in fact lower than the empirical value of $k_F \sim 1.35\ \mathrm{fm}^{-1}$.

In figs. 17a and b, we give the major partial wave contributions to PE/A of our ring diagram nuclear matter calculations using the Paris NN interaction. In figs. 17c and d the corresponding contributions are given for the Reid NN interaction. It is interesting to note that only the $^3S_1$-$^3D_1$ curves depict a saturation behavior. The overall nuclear matter saturation is governed by a delicate balance among these PE/A contributions and the kinetic energies at various k_F values. We note that the PE/A curves for the $^1S_0$, $^3S_1$-$^3D_1$, $^1P_1$ and $^3P_1$ of the Reid NN interaction are all significantly different from those of the Paris NN interaction.

The normalization condition of the Y-amplitudes, as given by eqs. (3.15) and (3.16), has played an important role in our nuclear matter calculations. As shown by eq. (4.16), $\Delta E_0^{pp}/A$ depends directly upon the Y-amplitudes, and the overall magnitudes of Y depend on the normalization constant Z_m of eqs. (3.15) and (3.16). From our discussion in sect. 4.2, it is easy to see that Z_m^{λ} of eq. (3.16) is approximately

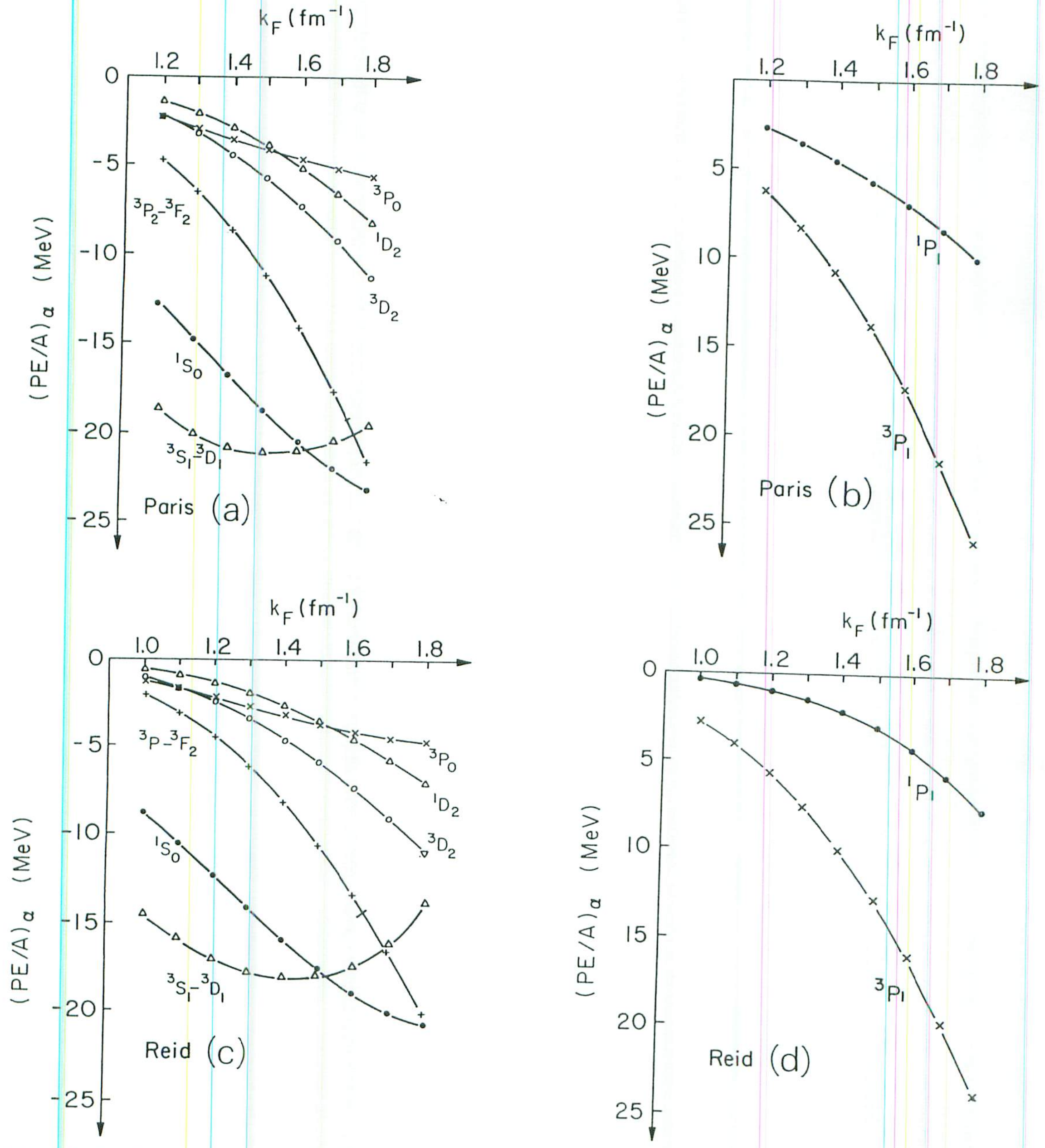

Fig. 17. Partial wave contributions to the potential energy per nucleon (PE/A) in our ring diagram nuclear matter calculations for the Paris (a, b) and Reid (c, d) NN interactions. $k_M = 3.2$ fm^{-1} is used.

equal to $(1+2\kappa^{(2)})^{-1}$ for $\lambda=0$ and 1 for $\lambda=0$, where typical values of $\kappa^{(2)}$ have been given in fig. 13. Note that λ is integrated from 0 to 1 as indicated by eq. (4.16). As expected, we have found that $\kappa^{(2)}$ generally increases with k_F. Namely, at higher k_F (i.e. higher density) $\kappa^{(2)}$ becomes larger and, consequently, Z_m^λ becomes smaller in general. Hence in eq. (4.16) the magnitudes of the Y-amplitudes become generally smaller, by a rather significant factor, as k_F increases. This has been an important factor in determining the saturation density of our nuclear matter calculations.

From the saturation curves of figs. 14 and 15, we have deduced the incompressibility coefficients

$$\boxed{K = k_{\mathrm{F}}^2 \frac{\mathrm{d}^2}{\mathrm{d}k_{\mathrm{F}}^2}\left(-\frac{\mathrm{BE}}{A}\right).} \tag{4.18}$$

They are 96.3 and 110.7 MeV for our ring diagram calculations using, respectively, the Paris and Reid NN potentials. Again, both the ring diagrams and the tensor force have played important roles in determining their values. We note that our value for the Reid case is in good agreement with the value recently suggested by Brown and Osnes [8]).

Finally, let us discuss an essential feature of our present nuclear matter theory. Our calculation is based on eq. (4.16), and to carry out its calculation we must first solve the RPA equation (4.10). Clearly this equation involves a non-Hermitian matrix and consequently its energy solutions may become complex. When this takes place, ΔE_0^{pp} of eq. (4.16) becomes generally complex and consequently nuclear matter becomes unstable. We have indeed found such complex solutions at $k_{\mathrm{F}} = 1.2\,\mathrm{fm}^{-1}$ for the Paris potential case (fig. 14) and at $k_{\mathrm{F}} = 1.0\,\mathrm{fm}^{-1}$ for the Reid potential case (fig. 15). (No complex solutions are found for all the other points of the RING curves of figs. 14 and 15.) Hence our calculation predicts nuclear matter instability at the above two situations. In the present work we have simply discarded the complex solutions of eq. (4.10), and the $k_{\mathrm{F}} = 1.0$ point of fig. 15 are obtained in this way. Nuclear matter instability is an important problem. [5]) It appears that our ring-diagram nuclear matter theory may provide a useful tool for studying this problem. We plan to carry out a more thorough investigation of the instability situation associated with complex solutions of eq. (4.10) in a future publication.

5. Discussion and conclusion

We have developed a new method for summing up the particle–particle ring diagrams of nuclear matter to all orders. This type of ring diagrams has not been investigated before. A desirable feature of our method is its relative simplicity for making calculations. One first chooses a model space, and calculates the model space reaction matrix G^{M} and s.p. spectrum. Using these, one solves a RPA-type secular equation to obtain the Y transition amplitudes. Then the potential energy of nuclear matter is given by simple integrals of the product $YY^{+}G^{\mathrm{M}}$.

Using the Paris and Reid NN potentials, we have applied the above method to nuclear matter calculations. The effects of the particle–particle ring diagrams are found to be rather important. Compared to the results of conventional BHF nuclear matter calculations, our calculations with the inclusion of the ring diagrams give a larger binding energy per nucleon as well as a *smaller* saturation density. It should be emphasized that we use a model-space s.p. spectrum which has self-energy insertions to particle lines (with momentum $k_{\mathrm{F}} < k < k_{\mathrm{M}}$). This enhances the effect of our ring diagrams as compared with the case where ring diagrams are calculated using a conventional discontinuous BHF s.p. spectrum.

Our calculations indicate that the ring diagrams are particularly important for the treatment of the NN tensor force. With these diagrams included, the NN tensor force has the clear tendency to make nuclear matter saturate at lower densities (as compared with nuclear matter calculations without the inclusion of the ring diagrams). This is a rather interesting result; it enables our nuclear matter result to move laterally away from the well-known Coester band [8]). In fact our calculated binding energy per nucleon and saturation density of nuclear matter, for both the Paris and Reid NN potentials, are both in rather satisfactory agreement with the corresponding empirical values as shown in figs. 14 and 15.

Our calculations can still be improved upon in several areas. Consequently, we do not want to emphasize the above good agreement between our results and the empirical nuclear matter properties. Instead, we wish to emphasize the trend provided by the inclusion of our ring diagrams in lowering the nuclear matter saturation densities. Shakin and his collaborators [14]) have pointed out that relativistic corrections are very important in lowering the nuclear matter saturation densities. Our calculations do not include relativistic corrections, yet our results have shown that the inclusion of our ring diagrams seems to have a rather strong effect in lowering the nuclear matter saturation density. This raises the intriguing possibility that the calculated nuclear matter saturation density may become too low if ring diagrams and relativistic corrections are both included. Further study in this direction is certainly needed. In fact, we are planning to carry out a ring diagram nuclear matter calculation with the inclusion of relativistic effects. Several authors [5,9,10]) have suggested the need of three-body effective interactions in lowering the calculated nuclear matter saturation density. Our calculations indicate that this need may be reduced by the inclusion of the ring diagrams.

We now discuss several aspects where the present calculation can be improved upon and where further investigations are needed. First, an important step of our calculation is the choice of k_M, the momentum space boundary of our model space. We have used $k_M = 3.2\ \mathrm{fm}^{-1}$. Our results clearly depend on the choice of k_M. Ma and Kuo [13]) have investigated the dependence of their MBHF calculations on the choice of k_M, and found that the dependence of their results on k_M was rather smooth. (They found a local minimum for BE/A at $k_M \approx 2k_F$.) Their calculations did not include the ring diagrams. Using their results as a guide line, we have used $k_M = 3.2\ \mathrm{fm}^{-1}$ in our present calculation. Limitations in computer time has prevented us from carrying out the present calculation using a series of different k_M values. This should be done in the future. In short, the choice of k_M is an uncertainty in the present calculation and should be further investigated.

Next, we turn to the angle-average approximations. As is well known, these approximations are standard (and indispensible) in treating the Pauli exclusion operators in the usual BHF nuclear matter calculations and are generally considered to be fairly accurate [1,2]). We have now generalized them to the treatment of the particle-particle RPA secular equations. This is done primarily because by doing so different partial waves are decoupled. Thus the calculation is greatly simplified. Although the approximations used in the RPA equations are very similar to those used in treating the Pauli operators in BHF calculations and we may expect them to have similar accuracies, it should still be very desirable to actually check the accuracy of the former. This may be done for restricted cases by solving the RPA equations directly in the laboratory frame by way of a vector-bracket transformation method [30]), and comparing the results so obtained with those obtained with the angle-average approximations.

Finally, we come to the particle-hole ring diagrams. As mentioned earlier, the YHK ring diagram method is applicable to the summation of the particle-hole ring diagrams. But their numerical calculation is actually more complicated than the particle-particle ring diagrams. This is because to calculate the particle-hole matrix element we need to make a transformation between the particle-hole channels and the particle-particle channels. Thus the various partial wave channels of the particle-particle interactions are generally coupled. The representation advocated by Dickoff, Faessler and Müther [31]) and by Müther [32]) appears to be a convenient way for studying the particle-hole ring diagrams. In fact they have calculated the particle-hole ring diagrams in nuclear matter using the Reid NN potential. There are, however, differences between their calculations and what we would like to calculate within the present framework.

As indicated in fig. 1, diagram (δ) is a third order particle-hole ring diagram. Diagram (β) may be treated as either a second-order particle-particle or as a second-order particle-hole ring diagram. We have used the former scheme and included diagram (β) in ΔE_0^{pp}. Thus, as discussed in ref. [15]), the lowest order particle-hole ring diagram in ΔE_0^{ph} - the potential energy contribution from the particle-hole ring diagrams - is *third* order in G^M. In contrast, the particle-hole ring diagrams of refs. [31,32]) and of Day's calculation [33]) begin with diagrams second order in the reaction matrix. There are indications that the particle-hole ring series converge rather rapidly and may not be very important for nuclear matter binding energy calculations [33,31,32]). Hence we expect that our ΔE_0^{ph} would be considerably less important than our ΔE_0^{pp}. This behavior has in fact been observed in some Lipkin model calculations [15]) and preliminary G-matrix calculations of the binding energy of ^{16}O [ref. [34])]. Whether the above expectation will be realized or not for nuclear matter remains to be investigated. Hence it will be worthwhile and interesting to actually calculate ΔE_0^{ph} for nuclear matter based on the framework of the present work and ref. [15]). Two further differences between ΔE_0^{ph} so calculated and earlier particle-hole ring diagram calculations [31-33]) are worth noting. First we employ a model-space approach which employs a self-consistent particle ($k_F < k < k_M$) spectrum whereas the earlier calculations employed a conventional BHF s.p. spectra. Second, our method for summing up the particle-hole ring diagrams will be similar to that given by eq. (3.13), and it will be considerably different from the methods used in earlier calculations. It will be of interest to investigate the effect of these differences on the role the particle-hole ring diagrams play in nuclear matter calculations.

The authors wish to thank Prof. G.E. Brown for many helpful discussions and encouragment throughout the course of this work. They are very grateful to Z.Y. Ma for several helpful correspondences and for making her MBHF computer programs available to them. They also wish to thank Prof. S.S. Wu for a number of helpful discussions and correspondences, to J. Heyer for a careful reading of the manuscript, and to Diane Siegel for her excellent and pleasant help in preparing the manuscript. Last but not least, H.Q.S. and S.D.Y. wish to thank Profs. G.E. Brown and A.D. Jackson for hospitality and support during their visit at Stony Brook.

References

1) H.A. Bethe, Ann. Rev. Nucl. Sci. **21** (1971) 93
2) D.W.L. Sprung, Adv. Nucl. Phys. **5** (1972) 225
3) J.P. Jeukenne, A. Lejeune and C. Mahaux, Phys. Reports **25C** (1976) 83
4) B.D. Day, Rev. Mod. Phys. **50** (1978) 495
5) A.D. Jackson, Ann. Rev. Nucl. Part. Sci. **33** (1983) 105
6) S.-O. Bäckman, G.E. Brown and J.A. Niskanen, Phys. Reports **124** (1985) 1
7) F. Coester, S. Cohen, B. Day and C.M. Vincent, Phys. Rev. **C1** (1970) 769
8) G.E. Brown and E. Osnes, Phys. Lett. **159B** (1985) 223
9) B.D. Day, Phys. Rev. Lett. **47** (1981) 226
10) T.T.S. Kuo, Z.Y. Ma and R. Vinh Mau, Phys. Rev. C **33** (1986) 717
11) H. Kümmel, K.H. Lührmann and J.G. Zabolitsky, Phys. Reports **36C** (1978) 1
12) R. Jastrow, Phys. Rev. **98** (1955) 1479; S. Fantoni and S. Rosati, Nuovo Cim. **A20** (1974) 179
13) Z.Y. Ma and T.T.S. Kuo, Phys. Lett. **B127** (1983) 137; T.T.S. Kuo and Z.Y.Ma, in Nucleon-nucleon interaction and nuclear many body problems, ed. S.S. Wu and T.T.S. Kuo (World Scientific, Singapore 1984), p. 178
14) M.R. Anastasio, L.S. Celenza, W.S. Pong and C.M. Shakin, Phys. Reports **100** (1983) 327
YHK-9 15) S.D. Yang, J. Heyer and T.T.S. Kuo, Nucl. Phys. **A448** (1986) 420
16) M. Lacombe, B. Loiseau, J.M. Richard, R. Vinh Mau, J. Coté, P. Pires and R. de Tourreil, Phys. Rev. **C21** (1980) 861
17) R.V. Reid, Ann. of Phys. **50** (1968) 411
18) See, for example, A.L. Fetter and J.D. Walecka, Quantum theory of many-particle systems (McGraw-Hill, 1971)
19) S.S. Wu and T.T.S. Kuo, Nucl. Phys. **A430** (1984) 110
20) S.D. Yang and T.T.S. Kuo, Nucl. Phys. **A456** (1986) 413
21) T.T.S. Kuo, Ann. Rev. Nucl. Sci. **24** (1974) 101; P.J. Ellis and E. Osnes, Rev. Mod. Phys. **49** (1977) 777
22) M. Haftel and F. Tabakin, Nucl. Phys. **A158** (1970) 1
23) G.E. Brown, A.D. Jackson and T.T.S. Kuo, Nucl. Phys. **A133** (1969) 481
24) E.M. Krenciglowa, C.L. Kung, T.T.S. Kuo and E. Osnes, Ann. of Phys. **101** (1976) 154
25) H.A. Bethe, B.H. Brandow and A.G. Petschek, Phys. Rev. **129** (1963) 225
26) B.D. Day and R.B. Wiringa, Phys. Rev. **C32** (1985) 1057
27) A. Lejeune, M. Martzolff and P. Grange, Lecture Notes in Physics (Springer) vol. 198 (1984) 36
28) M.A. Matin and M. Dey, Phys. Rev. **C27** (1983) 2356: **C29** (1984) 344(E)
29) T.T.S. Kuo and G.E. Brown, Phys. Lett. **18** (1965) 54

30) See, for example, C.L. Kung, T.T.S. Kuo and K.F. Ratcliff, Phys. Rev. **C19** (1979) 1063
31) W.H. Dickoff, A. Faessler and H. Müther, Nucl. Phys. **A389** (1982) 492
32) H. Müther, Nucleon-nucleon interaction and nuclear many body problem ed. S.S. Wu and T.T.S. Kuo (World Scientific, 1984) p. 490.
33) B.D. Day, Phys. Rev. **C24** (1981) 1203
34) H. Müther and T.T.S. Kuo, private communication